Interplay of chordwise stiffness and shape on performance of self-propelled flexible flapping plate

Wenjiang Wang, Haibo Huang, and Xi-Yun Lu

View Online   Export Citation   CrossMark

Interplay of chordwise stiffness and shape on performance of self-propelled flexible flapping plate

View Online   Export Citation   CrossMark

Wenjiang Wang,[1,2] (iD) Haibo Huang,[1] (iD) and Xi-Yun Lu[1,a] (iD)

AFFILIATIONS

[1]Department of Modern Mechanics, University of Science and Technology of China, Hefei, Anhui 230026, China
[2]Shenzhen Institutes of Advanced Technology, Chinese Academy of Sciences, Shenzhen, Guangdong 518055, China

[a]Author to whom correspondence should be addressed: xlu@ustc.edu.cn

ABSTRACT

The locomotion of a flapping flexible plate with different shapes and non-uniform chordwise stiffness distribution in a stationary fluid is studied numerically. The normalized effective bending stiffness K^* for three-dimensional plates with arbitrary stiffness distribution and shape parameters is proposed, and the overall bending stiffness of non-uniform plates with different shapes is reasonably characterized. It is found that the propulsion performance in terms of cruising speed and efficiency of the self-propelled flapping plate mainly depends on the effective bending stiffness. Plates with moderate flexibility K^* show better propulsion performance. Meanwhile, both a large area moment of the plate and a flexible anterior are favorable to significantly improve their propulsive performance. The evolution of vortical structures and the pressure distribution on the upper and lower surfaces of the plate are analyzed, and the inherent mechanism is revealed. These findings are of great significance to the optimal design of propulsion systems with different fins or wings.

I. INTRODUCTION

Through several hundred million years of evolution and natural selection, organisms in nature, such as birds and fish, have obtained superior propulsion performance and high mobility to meet their expected survival needs. These features are realized by flapping wings or fins with various shapes and flexibility in different flying and swimming organisms.[1–5] The optimal combination of geometry and material structure parameters of biological propellers may significantly enhance their propulsive performances, whose study may provide inspiration for the design and improvement of new underwater vehicles.[6,7]

The effect of fin flexibility on its propulsion and handling performance has been investigated with particular focus on flapping plates by constructing a suitable flapping plate model and assuming that the biological structure is a homogeneous material combined with theoretical analysis,[8–10] experimental observation,[11–13] and numerical simulation.[8,14–19] The results show that flapping flexible plates are superior to rigid plates in regard to propulsion speed and efficiency. However, the structure and material properties of actual organisms are complex, and the wings of birds or fins of fish are usually anisotropic and

heterogeneous.[20] McHenry *et al.*[21] measured the bending stiffness of sunfish along their body axis, and found that the caudal fin stiffness decreased exponentially. Zuo and Jiang[22] treated the fish to death, fixed the front part on a horizontal plate with a clamp, and the back part hung on a horizontal edge so as to bend freely under the action of gravity. Then, the bending curvature of different parts was analyzed by a quadratic polynomial function, and the results showed that the tangential bending stiffness of the fish decreased from beginning to end. Kancharala and Philen[23] measured the bending stiffness of the caudal fin of three kinds of fish (trout, red snapper, red snapper) at the same time, and found that the fin stiffness profile is similar to the predicted theoretical optimization profile, that is, the leading edge has a higher stiffness, and that of the trailing edge gradually decreases.

In recent years, a series of anatomical measurements, model experiments, and numerical simulations have promoted research on the hydrodynamic performance of flexible propellers with non-uniform stiffness distribution. It is worth noting that their chord stiffness distribution may be more important than their spanwise stiffness, because the flow and autonomous propulsion are along the chord direction, so the related propulsion performance deserves more attention. Luo *et al.*[24] studied the influence of chord and spanwise stiffness

distribution on the propulsion performance of tuna, and the results confirmed that the chord stiffness was dominant. By changing the thickness of the flexible plate model to generate discrete regions with high flexibility and low flexibility and comparing the effects of different stiffness distributions on the swimming performance, Zhu et al.[25,26] found that the tangential non-uniform stiffness distribution is better than the spanwise distribution in regard to thrust and efficiency. Fernández-Gutiérrez and van Rees[27] proposed a simplified leading edge curvature driven model to simulate the passive elastic deformation and active curvature of thin films under external hydrodynamic loads, and to calculate the thrust and power. Their results show that improvement in propulsion performance is mainly caused by the trailing edge motion due to the curvature of the leading edge. When the trailing edge is fixed, the change of fin camber is beneficial to improve the propulsion efficiency. Due to the complexity of structural materials and the lack of appropriate analysis methods to evaluate the overall stiffness of non-uniform flexible plates, views on optimal stiffness distribution are always contradictory in the literature and need to be resolved. Lucas et al.[28] found that flapping plates with non-uniform stiffness distribution can achieve faster propulsion speed and lower energy-efficiency ratio. Moore[29] numerically studied the influence of different chord stiffness distributions on the propulsive performance of two-dimensional flapping plates. The results show that the torsional spring stiffness distribution (leading edge stiffness weakening) is the optimal distribution which can significantly improve the propulsion performance of the plate. On the other hand, some researchers believe that flexible flapping wings with enhanced leading edge stiffness have higher average lift–drag ratio and lift–power ratio.[30–33] According to a series of typical stiffness distributions, Wang et al.[34] derived the effective bending stiffness for the first time, systematically studied the propulsion characteristics and flow mechanism of flexible plate, and found that flapping flexible plates with increasing stiffness along the chord direction had better propulsion performance, but only rectangular plates were considered in the study. Shi et al.[35] numerically investigated the effects of time-varying bending stiffness on the propulsion performance of a flapping foil and found that the maximum time-averaged thrust coefficient can be increased by 52% whereas the highest propulsion efficiency remains almost the same as that of the foil with constant flexibility.

In fact, similar to the structural features of organisms, the morphological characteristics of different propellers vary greatly to adapt to the characteristics of their respective modes of motion.[36] In recent years, some researchers have chosen the rigid model based on the real fish configuration for experimental, theoretical, and numerical research, and have further considered the influence of propeller shape design on biological propulsion performance.[4,37–40] Chopra and Kambe[41] studied the effect of plane shape on the caudal fin of fish in inviscid flow, and gave the functional relationship between thrust and efficiency when the circular leading edge, sharp trailing edge, and aspect ratio changed. Green et al.[42] used particle image velocimetry (PIV) to study the three-dimensional (3D) wake vortices of rigid pitching plates with trapezoidal geometry to simulate the fish caudal fin. Experimental results show that a trapezoidal geometry generates additional vortices along the swept edge, and the complexity of the wake increases with the lateral expansion of spanwise vortices at higher Strouhal numbers. Li et al.[43] compared the effects of caudal fin shape on propulsion performance of three fish species with different

bifurcations. By changing the flapping amplitude of the combined pitching and heaving motion, it is found that the shape of the caudal fin of carangiformes is conducive to the generation of thrust, while the crescent caudal fin of thunniform can significantly improve their efficiency. Van Buren et al.[36] experimentally studied the effect of trailing edge shape on the propulsion performance of flapping plates. Their results show that the time-averaged velocity field changes significantly by changing the wake vortex structure. In terms of performance, the trailing edge from concave to convex, thrust, and efficiency are generally improved.

Combination of the benefits of flexible deformation and shape change may further enhance propulsion performance.[44–46] At present, research work in this topic is relatively less. Lauder et al.[47] studied the influence of the trailing edge shape of flapping plates with high flexibility under very high aspect ratio (e.g., eel), and found that changing the trailing edge shape can significantly improve the cruising speed of the flexible plate. Ryu et al.[48] simulated flexible plates with different shapes, and found that when the shape ratio (the ratio of trailing edge length to leading edge length) was 0.5, the best propulsion efficiency was achieved. Zhang et al.[49] numerically studied the self-propulsion of flexible plates with different trailing edges. The results show that the propulsion characteristics of flexible plates with different bending stiffness vary with the shape of trailing edge. However, the physical models of the above research work are homogeneous materials, and real chordwise flexible distribution is not considered. In summary, exploring the influence of specific shape design and flexible distribution of organisms independently may not be sufficient. An optimal combination of propeller shape design and flexible distribution may enhance their propulsive performance significantly.

In the present study, we carried out numerical simulations on the locomotion of self-propelled three-dimensional (3D) flexible plates with varying non-uniformly distributed stiffness and shape parameter. Based on the equivalent global stiffness of rectangular plates summarized in a previous work,[34] the effects of different bending stiffness and shape parameters on the propulsion performance of a series of typical flexible plates are studied, and the tangential deformation, pressure distribution, near-field vortex structure and strength, as well as the normal force on the plate are analyzed. Furthermore, the internal relationship between the specific shape and flexible design of biology and the propulsion performance of caudal fin is revealed.

The remainder of this paper is organized as follows: The physical problem and mathematical formulation are presented in Sec. II. The numerical method and validation are described in Sec. III. Results are discussed in Sec. IV and concluding remarks are addressed in Sec. V.

II. PHYSICAL PROBLEM AND MATHEMATICAL FORMULATION

As shown in Fig. 1(a), a 3D flexible plate with chord length c is immersed in a stationary fluid and is symmetrical along the spanwise direction (z) where θ represents the angle of the trailing edge. When $\theta = 90°$, the plate is square. In the present study, equivalent aspect ratio is defined as $AR = (b_1 + b_2)/2c$, where b_1 and b_2 are the spanwise length of the leading edge and trailing edge, respectively. In all cases, $AR = 1$. The leading edge of the plate is forced to heave sinusoidally with oscillating amplitude a_0 and frequency f in the vertical direction. The actuation of the leading edge is described as[50,51]
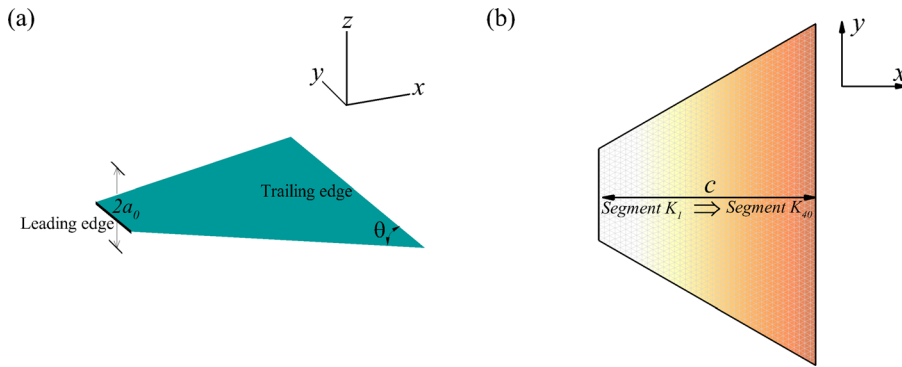
FIG. 1. (a) Schematic diagram of a 3D flexible plate. The leading edge is forced to heave vertically and sinusoidally. The plate deforms passively and moves forward freely; (b) the generated meshes for the plate with 40 segments in different colors.

$$a(t) = a_0 \cos(2\pi f t). \tag{1}$$

As a result of the interplay of the plate elasticity, leading edge forcing, and the forces exerted by the surrounding fluid, the plate can move forward freely and passively in a stationary fluid. Meanwhile, only the leading edge of the plate is restricted with a prescribed vertical motion, the remainder of the plate can move freely in the entire fluid domain. Here, a Lagrangian coordinate system (s_1, s_2) along the plate surface is defined to describe the configuration and motion of the plate. The fluid flow is governed by the incompressible Navier–Stokes equations as follows:

$$\frac{\partial v}{\partial t} + v \cdot \nabla v = -\frac{1}{\rho}\nabla p + \frac{\mu}{\rho}\nabla^2 v + f, \tag{2}$$

$$\nabla \cdot v = 0, \tag{3}$$

where v is the velocity, p is the pressure, ρ is the density of the fluid, μ is the dynamic viscosity, and f is the Eulerian force acting on the surrounding fluid due to the immersed boundary (IB), as constrained by the no-slip boundary condition. The structural equation is employed to describe the deformation and motion of the plate as follows:[52,53]

$$\rho_s h \frac{\partial^2 X}{\partial t^2} = \sum_{i,j=1}^{2}\left[\frac{\partial}{\partial s_i}\left(\varphi_{ij}\left(\delta_{ij} - \left(\frac{\partial X}{\partial s_i}\cdot\frac{\partial X}{\partial s_j}\right)^{-1/2}\right)\frac{\partial X}{\partial s_j}\right)\right.$$
$$\left. -\frac{\partial}{\partial s_j}\left(\gamma_{ij}\frac{\partial^2 X}{\partial s_i \partial s_j}\right)\right] + F, \tag{4}$$

where $X = (X, Y, Z)$ is the position vector of the plate, F_s is the Lagrangian force exerted on the plate by the fluid, ρ_s is the structural mass density of the plate, and h is the thickness of the plate. φ_{ij} is the in-plane effect matrix, where $\varphi_{11} = \varphi_{22} = Eh$ is the stretching stiffness and $\varphi_{12} = Gh$ is the shearing stiffness of the plate. γ_{ij} is the out-of-plane effect matrix, where $\gamma_{11} = \gamma_{22} = \gamma_{12} = EI$ is the bending stiffness of the plate. Besides, δ_{ij} is the Kronecker delta function.

At the leading edge of the plate, the clamped boundary condition is adopted, i.e.,

$$\varphi_{ij}\left(\delta_{ij} - \left(\frac{\partial X}{\partial s_i}\cdot\frac{\partial X}{\partial s_j}\right)^{-1/2}\right)\frac{\partial X}{\partial s_j} - \frac{\partial}{\partial s_j}\left(\gamma_{ij}\frac{\partial^2 X}{\partial s_i \partial s_j}\right) = 0, \tag{5}$$

$$Y(t) = Y(0), \quad Z(t) = a(t), \quad \frac{\partial X}{\partial s_1} = (1, 0, 0). \tag{6}$$

For the free end of the plate, the boundary condition is

$$\varphi_{ij}\left(\delta_{ij} - \left(\frac{\partial X}{\partial s_i}\cdot\frac{\partial X}{\partial s_j}\right)^{-1/2}\right)\frac{\partial X}{\partial s_j} - \frac{\partial}{\partial s_j}\left(\gamma_{ij}\frac{\partial^2 X}{\partial s_i \partial s_j}\right) = 0, \tag{7}$$

$$\frac{\partial^2 X}{\partial s_i \partial s_j} = 0. \tag{8}$$

The two other free edges $s_2 = 0$ or b are imposed. Here, the Einstein summation convention is not applied on i and j $(i, j = 1, 2)$.

The chord length of the plate c, the heaving frequency f, and the fluid density ρ are used as characteristic quantities to normalize the above equations. It is noted that the characteristic time is $1/f$, i.e., the heaving period. Based on non-dimensional analysis, there are several dimensionless parameters in our problem: the Reynolds number $Re = \rho f c^2 / \mu$, the stretching stiffness $S = Eh/\rho f^2 c^3$, the bending stiffness $K = EI/\rho f^2 c^5$, the mass ratio of the plate and the fluid $M = \rho_s h/\rho c$, the heaving amplitude $A = a_0/c$ and the aspect ratio of the plate $AR = (b_1 + b_2)/2c$. In addition, the characteristic time is $T = 1/f$, i.e., the flapping period of the plate.

According to the shape of fish caudal fin, the more basic geometry is abstracted and five typical planes are studied. To describe the different plate shapes, the area moments are used to distinguish them quantitatively. Following a description of morphological parameters for the insect wings,[54] the first non-dimensional radius of the area moment is defined as

$$\hat{r} = \frac{A_1}{Ac}, \tag{9}$$

where $A_1 = \int_0^c y(x)x\,dx$ is the first area moment, the span $y(x)$ is a function of the chord distance x, and $A = 1$ is the dimensionless area of the plate. For five typical plates, their first area moments are given in Table I. It is worth noting that $0.4 \lesssim \hat{r} \lesssim 0.6$ represents the major range of the area moment of the wings and fins of flying and swimming animals.[55] It means that the range of $\hat{r}$ considered in this study covers the regime of biological observation.

TABLE I. Radii of the area moments of the typical plates.

θ	60°	75°	90°	105°	120°
$\hat{r}$	0.596	0.545	0.5	0.455	0.404

To model the non-uniformly distributed stiffness in the present three-dimensional model, the plate is structurally composed of 40 segments in the chordwise direction. Each segment is assigned a unique $K_i = E_i I / \rho f^2 c^5$, as shown in Fig. 1(b). In our study, the distributions of K are considered as follows:

1. Uniform distribution: $K_i = \bar{K}$;
2. Exponential distribution: $K_i = \bar{K} R_i / R$, $R_i = e^{-q\frac{i}{N}}$, and $e^{-q\frac{N-i}{N}}$ for the DD and GD cases, respectively.

Here, DD and GD denote the declining and growing distributions, respectively, from the leading to the trailing edge of the plate. Figure 2 shows the variation of different bending stiffness distributions along the chord direction. $\bar{K}$ is the arithmetic mean stiffness of all the segments and $q = 1, 3.698$; $R = \int_0^1 e^{(-qx)} dx$. To describe the different stiffness distributions more concisely, the symbols $\downarrow$ and $\uparrow$ denote the DD and GD cases, respectively. The symbol $exp1$ indicates $q = 1$, $exp2$ for $q = 3.698$.

III. NUMERICAL METHOD AND VALIDATION

The governing equations of the fluid-plate problem are solved numerically by an immersed boundary-lattice Boltzmann method for the fluid flow[56] and a finite element method for the motion of the flexible plates.[57] The immersed boundary (IB) method has been extensively applied to problems involving moving boundaries immersed in a viscous fluid flow.[58,59] When the IB method is used to resolve flow–structure interaction, the Lagrangian interaction force F_s in Eq. (4) between the fluid and the immersed boundary can be calculated by the feedback law,[58,59]

$$\mathbf{F}_s(s_1, s_2, t) = \alpha \int_0^t \left[\mathbf{V}_f(s_1, s_2, t') - \mathbf{V}_s(s_1, s_2, t') \right] dt' + \beta \left[\mathbf{V}_f(s_1, s_2, t) - \mathbf{V}_s(s_1, s_2, t) \right], \quad (10)$$

where α and β are free parameters and are selected based on Ref. 53, $V_s = \frac{\partial X}{\partial t}$ is the plate velocity and the fluid velocity V_f at X is interpolated from the velocities of the surrounding fluid nodes v,
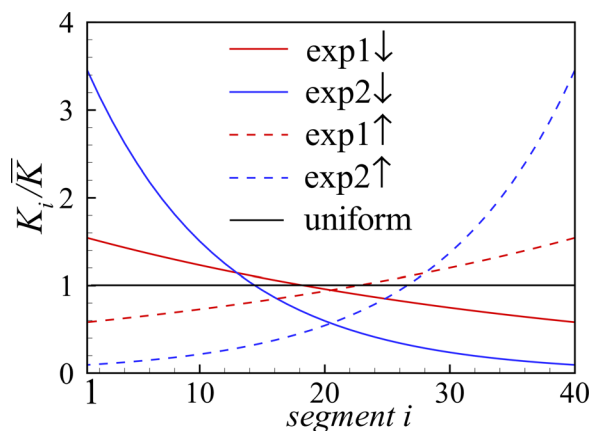

FIG. 2. Distribution patterns of stiffness, where the black line represents the uniform distribution case.

$$V_f(s_1, s_2, t) = \int v(x, t) \delta(\boldsymbol{x} - \boldsymbol{X}(s_1, s_2, t)) d\boldsymbol{x}. \quad (11)$$

In the IB scheme, due to the presence of the plate, the body force f would be exerted on the fluid nodes. In this way, the no-slip boundary condition on the moving plate would be satisfied. The body force f on the Eulerian points (fluid nodes) can be obtained from the Lagrangian force F_s using the Dirac delta function as follows:[58]

$$\boldsymbol{f}(x, t) = -\int \boldsymbol{F}_s(x, t) \delta(\boldsymbol{x} - \boldsymbol{X}(s_1, s_2, t)) ds_1 ds_2. \quad (12)$$

Furthermore, the lattice Boltzmann equation (LBE) has been widely used to simulate complex flows as an alternative to conventional numerical methods for the Navier–Stokes equations.[51,53,56,60,61] The LBE with the BGK model is

$$f_i(\boldsymbol{x} + \boldsymbol{e}_i \Delta t, t + \Delta t) - f_i(\boldsymbol{x}, t) = -\frac{1}{\tau} \left[f_i(\boldsymbol{x}, t) - f_i^{eq}(\boldsymbol{x}, t) \right] + \Delta t F_i, \quad (13)$$

where τ is the non-dimensional relaxation time related to fluid viscosity, Δt is the time step, and $f_i(\boldsymbol{x}, t)$ is the distribution function associated with discrete particle velocity $\boldsymbol{e}_i$. The equilibrium distribution function f_i^{eq} and the forcing term F_i[62] are defined as

$$f_i^{eq} = \omega_i \rho \left[1 + \frac{\boldsymbol{e}_i \cdot \boldsymbol{v}}{c_s^2} + \frac{\boldsymbol{v}\boldsymbol{v} : (\boldsymbol{e}_i \boldsymbol{e}_i - c_s^2 \boldsymbol{I})}{2c_s^4} \right], \quad (14)$$

$$F_i = \left(1 - \frac{1}{2\tau} \right) \omega_i \left[\frac{\boldsymbol{e}_i - \boldsymbol{v}}{c_s^2} + \frac{\boldsymbol{e}_i \cdot \boldsymbol{v}}{c_s^4} \boldsymbol{e}_i \right] \cdot \boldsymbol{f}, \quad (15)$$

where ω_i is the weighting factor and c_s is the sound speed. The macro-variables velocity v and mass density ρ can be obtained through the distribution functions,

$$\rho = \sum_i f_i, \quad \rho v = \sum_i \boldsymbol{e}_i f_i + \frac{1}{2} \boldsymbol{f} \Delta t. \quad (16)$$

Equation (4) for a deformable plate is discretized by a finite element method and the deformation with large displacement of the plate is handled by the co-rotational scheme.[57] A detailed description of the numerical method can be found in our previous papers.[53,63] A finite moving computational domain is used in the x-direction to allow the plate to move for a sufficiently long time. As the plate travels one lattice in the x direction, the computational domain is shifted, i.e., one layer is added at the inlet and another layer is removed at the outlet. A non-uniform mesh technique is employed to solve our problem for improving the computational efficiency. Based on our careful validations shown below, the computational domain for the fluid flow is chosen as $[-10, 30] \times [-10, 10] \times [-10, 10]$ in the x, y, z directions, which is large enough so that the blocking effects of the boundaries are small enough. In the simulations, the Neumann boundary condition $\partial v / \partial x = 0$ is applied at the outlet and the Dirichlet boundary condition $v = 0$ is applied at the inlet and the other four boundaries.

To validate the numerical method used in the present study, a flapping flag in a uniform incoming flow was simulated. The key parameters are $Re = 100$, $M = 1$, $H = 1$, $S = 1000$, and $K = 0.0001$, which are identical to those in Huang and Sung.[64] Figure 3(a) shows a comparison of the present results and data provided in the literature.
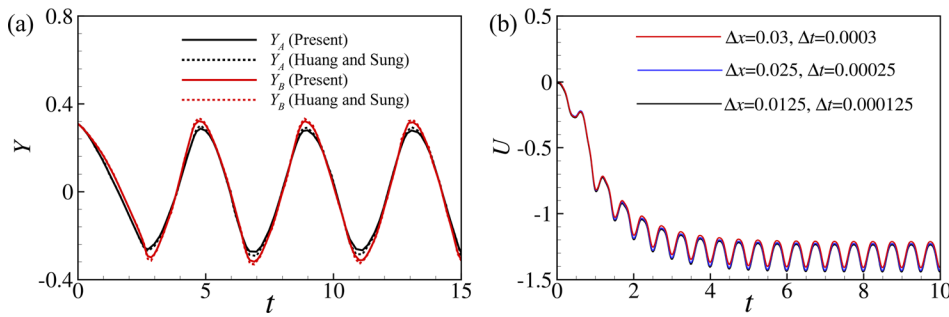
FIG. 3. (a) Time-dependent transverse (y direction) displacements at points A (low corner on the trailing edge) and B (mid-point on the trailing edge). (b) Cruising speed of the flapping flexible plate as a function of time ($A = 0.2$, $M = 0.5$, $K = 2$, $H = 1$, and $Re = 100$).

It is seen that both time-dependent transverse (y direction) displacements at points A (low corner on the trailing edge) and B (mid-point on the trailing edge) in our simulation agree well with those in Huang and Sung.[64]

Grid independence and time step independence studies were also performed. A typical case of a flexible plate with uniform stiffness was simulated, with parameters $A = 0.2$, $M = 0.5$, $K = 2$, $H = 1$, and $Re = 100$. The propulsive velocity of the cases with different mesh size and time step size is shown in Fig. 3(b). It is seen that $\Delta x/L = 0.025$ and $\Delta t = 0.000\,25$ are sufficient to achieve accurate results. Here, in all our simulations, $\Delta x/L = 0.025$ and $\Delta t = 0.000\,25$ are adopted.

Our numerical strategy has been validated and successfully applied to a wide range of flows, such as the collective locomotion of two closely spaced self-propelled flapping plates,[51] the self-propulsion of 3D flexible plates with different trailing-edge shapes,[49] and optimal chordwise stiffness distribution for self-propelled heaving flexible plates.[34]

IV. RESULTS AND DISCUSSION

We present some results on the propulsive behaviors of three-dimensional flexible trapezoidal plates with non-uniform stiffness distribution. Their parameters are shown in Table II. It is seen that the Reynolds number Re, the stretching stiffness S, the mass ratio M, and the flapping amplitude A are fixed in our study. The following three parameters are variables: arithmetic mean bending stiffness $\bar{K}$, stiffness distribution, and plane shape parameter.

A. Propulsive performance

To quantify the propulsive performance of the plates, the mean propulsive velocity, input work, and propulsive efficiency are evaluated. The mean propulsive velocity U is the time-averaged cruising speed at equilibrium. Figure 4 shows the propulsive velocity U as a

TABLE II. Parameters in the simulations.

Reynolds number	Re	100
Mass ratio	M	0.5
Stretching stiffness	S	1000
Arithmetic mean bending stiffness	$\bar{K}$	[0.5, 80]
Flapping amplitude	A	0.25
Trailing edge angle	θ	[60°, 120°]

function of the arithmetic mean bending stiffness $\bar{K}$ for plates with different stiffness distributions and shape parameter, i.e., trailing edge angle θ. The case of a uniform plate is also illustrated for comparison. It can be seen that overall, for a flapping plate with a specific shape parameter, U first increases and then decreases with $\bar{K}$ and there is a peak at a specific $\bar{K}$. The result looks similar to that of the rectangular uniform plate in Ref. 34. It is also seen that when the stiffness distribution changes from the DD mode to uniform plate and then to the GD mode, the curve of propulsive velocity U gradually shifts to the right, and the peak of U increases. Under the same $\bar{K}$, the flexible plates with different stiffness distribution show different trends of propulsion velocity. On the other hand, for any specific stiffness distribution, with increase in θ, the curve of U moves to the left gradually. The peak value of maximum propulsion speed for a plate with acute θ is better than that with obtuse θ.

The input work W, which is required to actuate the leading edge of the plate, is the time integral of the power P over the surface of the plate in the surrounding fluid during one flapping period T,

$$W = \int_{t'}^{t'+T} P(t)dt = \int_{t'}^{t'+T} \left[\int_0^1 \mathbf{F}_r(s_1, s_2, t) \cdot \frac{\partial \mathbf{X}(s_1, s_2, t)}{\partial t} ds_1 ds_2 \right] dt, \quad (17)$$

where $\mathbf{F}_r$ is the force on the surrounding fluid by the plate. The propulsive efficiency η is usually defined as the ratio between the kinetic energy of the plate and the input work, i.e.,

$$\eta = \frac{1}{2} MU^2/W. \quad (18)$$

The propulsive efficiency η as a function of $\bar{K}$ and geometry parameter θ is shown in Fig. 5. Generally speaking, the variation trends of η with $\bar{K}$ are consistent with that of U. Besides, the corresponding $\bar{K}$ when η reaches a peak is identical to that of U.

On the one hand, when the stiffness distribution gradually changes from the DD mode to the uniform plate and then to the GD mode, the curves of U or η move to right and the peaks increase gradually, especially "exp2 ↑." Under the same $\bar{K}$, the flexible plates with different stiffness distribution show different propulsion performance trends. On the other hand, for any specific stiffness distribution, with increase in the trailing edge angle θ, the U or η curves move left in the $U - \bar{K}$ or $\eta - \bar{K}$ planes. The peak of U or η of the acute angle is better than that of the obtuse angle. Therefore, $\bar{K}$ is not appropriate to describe the overall bending stiffness of plates with different shapes
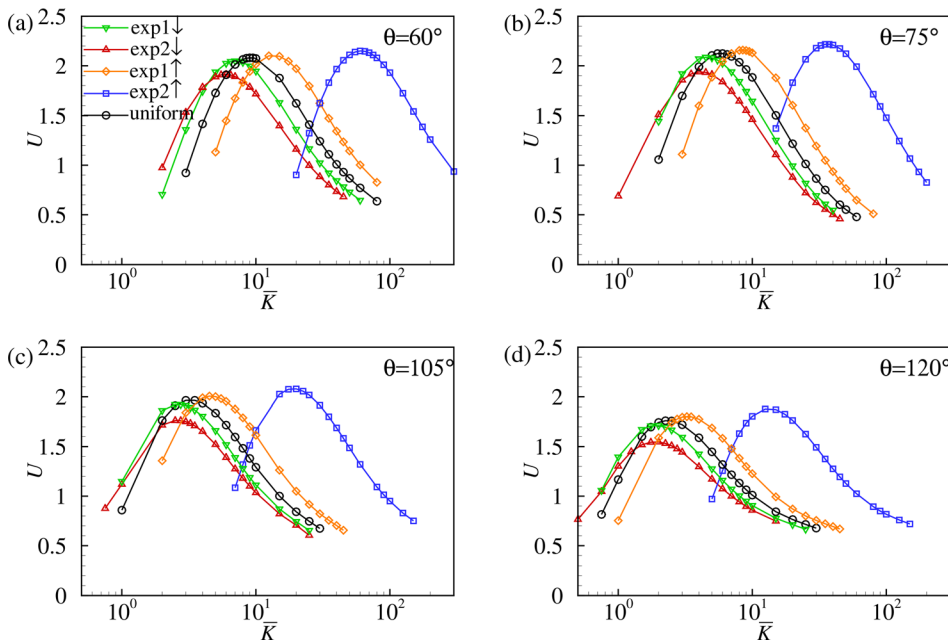
FIG. 4. Propulsive velocity U as a function of mean bending stiffness $\bar{K}$ of the plate under different stiffness distributions and shape parameter θ: (a) $\theta = 60°$, (b) $\theta = 75°$, (c) $\theta = 105°$, and (d) $\theta = 120°$.

and non-uniform distributions, especially for GD mode. In addition, shape parameters play an important role in the propulsion performance of the plate. The arithmetic mean stiffness $\bar{K}$ is not able to incorporate the effect of shape parameters.

B. Normalized bending stiffness $\tilde{K}$

In this section, here another appropriate overall bending stiffness of flexible plate K^* is well defined. It is based on the effective bending

stiffness of the rectangular plate derived in Ref. 34 but the shape parameters are well incorporated. We suppose that when the overall bending stiffness of the plate is identical, regardless of the stiffness distribution and shape parameters, the deflection at the end of the plate should be the same if the same load is applied. In fact, when the spanwise section shape of a flapping flexible plate changes little, it still can be regarded as a Euler beam with one end fixed and the other free. According to the approximate differential equation of the deflection curve, we have
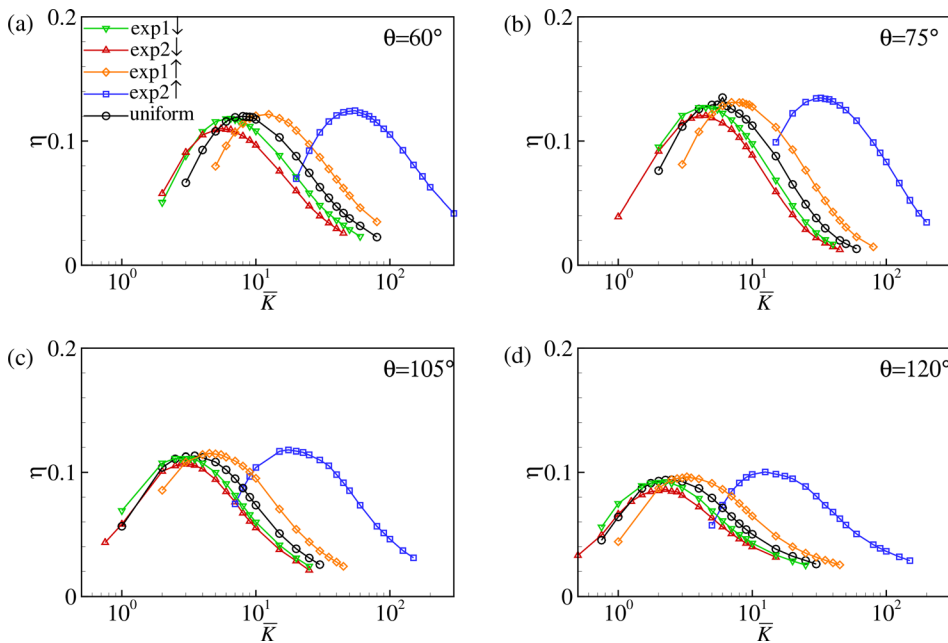

FIG. 5. Propulsive efficiency η as a function of mean bending stiffness $\bar{K}$ and shape parameter θ: (a) $\theta = 60°$, (b) $\theta = 75°$, (c) $\theta = 105°$, and (d) $\theta = 120°$.

$$E(x)I(x)\frac{\partial^2 w(x)}{\partial x^2} = -M(x), \quad x \in [0,1], \tag{19}$$

where $E(x)I(x)$ represents the chordwise bending stiffness distribution with x being the chordwise position, $w(x)$ is the deformed deflection of the plate, and $M(x)$ is the internal moment. It should be noted that Young's modulus $E(x)$ and section moment of inertia $I(x)$ both change with chord position x. The forces experienced by flapping plates in a viscous incompressible fluid is complex. Previous studies[49,51] have indicated that the bending deformation of a flapping plate is mainly contributed by the normal force. Peng et al.[51] have shown that the time-averaged absolute normal force of a heaving flexible plate approximately decreases linearly from the leading to the trailing edges. For simplicity, the load distribution along the chordwise direction is supposed to be the normal force distribution. Here, a unified linear decreasing load distribution is used, where q_0 is the normal force value at the leading edge and 0 at the trailing edge. For the beam, the boundary conditions at the leading edge are

$$x = 0, \quad w = 0, \quad \frac{\partial w}{\partial x} = \phi = 0, \tag{20}$$

where ϕ is the deflection angle.

Integrating Eq. (19), we can obtain the tail deformed deflection angle,

$$\phi(1) = \frac{\mathrm{d}w}{\mathrm{d}x} = \int_0^1 \frac{-M(x)}{E(x)I(x)}\mathrm{d}x + C. \tag{21}$$

Integrating Eq. (19) twice, we obtain the tail deformed deflection,

$$w(1) = \int_0^1 \int_0^x \left(\frac{-M(x')}{E(x')I(x')}\mathrm{d}x' \right)\mathrm{d}x + Cx + D, \tag{22}$$

where C and D are integral constants.

For all stiffness distribution and shape parameters of flexible plates, the bending moment $M(x)$ is

$$M(x) = -\frac{q_0}{6}(1-x)^3, \quad x \in [0,1]. \tag{23}$$

For a rectangular plate with uniform stiffness, the moment of inertia of the cross section is $I(x) = \frac{h^3}{12}$, and the analytical solution of the tail's deformed deflection is

$$w(1) = \frac{q_0}{30\bar{K}}. \tag{24}$$

For other plates with different shapes denoted by θ, the moments of inertia of the section are

$$I(x) = \begin{cases} \frac{h^3}{12} \cdot \left(1 - \frac{1}{\sqrt{3}} + \frac{2x}{\sqrt{3}}\right), & \theta = 60°, \\ \frac{h^3}{12} \cdot \left(1 - \frac{1}{2+\sqrt{3}} + \frac{2x}{2+\sqrt{3}}\right), & \theta = 75°, \\ \frac{h^3}{12} \cdot \left(1 + \frac{1}{2+\sqrt{3}} - \frac{2x}{2+\sqrt{3}}\right), & \theta = 105°, \\ \frac{h^3}{12} \cdot \left(1 + \frac{1}{\sqrt{3}} - \frac{2x}{\sqrt{3}}\right), & \theta = 120°. \end{cases} \tag{25}$$

For the non-rectangular flexible plate with non-uniform stiffness distribution, two typical examples are selected to explain in detail.

For the typical DD mode and $\theta = 60°$ case ($q = 1$),

$$E(x)I(x) = \bar{K}\frac{e^{-x}\left(1 - \frac{1}{\sqrt{3}} + \frac{2x}{\sqrt{3}}\right)}{\int_0^1 e^{-x}\mathrm{d}x}, \quad x \in [0,1]. \tag{26}$$

It yields $w(1) = \frac{q_0}{33.4821\bar{K}}$.

Similarly, for the typical GD mode and $\theta = 60°$ case ($q = 1$),

$$E(x)I(x) = \bar{K}\frac{e^{1-x}\left(1 - \frac{1}{\sqrt{3}} + \frac{2x}{\sqrt{3}}\right)}{\int_0^1 e^{1-x}\mathrm{d}x}, \quad x \in [0,1]. \tag{27}$$

Then, $w(1)$ can be derived as $\frac{q_0}{17.9104\bar{K}}$. Therefore, the general form of a tail deformed deflection of flexible plate with arbitrary shape is

$$w(1) = \frac{q_0}{\mu\bar{K}}, \tag{28}$$

where μ is a coefficient for a particular shape and stiffness distribution case. Now, suppose in all cases, the deformed deflection at the trailing edge has the same formula as that of a uniform rectangular plate

$$w(1) = \frac{q_0}{30K^*}, \tag{29}$$

where K^* is the overall bending stiffness. It is noticed that for the uniform rectangular plate, $K^* = \bar{K}$. From Eqs. (28) and (29), it follows that

$$K^* = \frac{\mu\bar{K}}{30}. \tag{30}$$

Through the parameter μ, the expression of deformed deflection of a flexible plate with arbitrary shape under all stiffness distributions is transformed into the form of uniform rectangular plate. Therefore, K^* is a normalized overall bending stiffness, i.e., an effective bending stiffness.

The corresponding relationship between the effective bending stiffness K^* and the arithmetic mean stiffness $\bar{K}$ of flexible plates with arbitrary shape under all non-uniform stiffness distributions is shown in Table III. It is seen that for a specific shape of flexible plate, the effective bending stiffness K^* decreases gradually from the DD mode to uniform plate and then to the GD mode. On the other hand, for any specific stiffness distribution, the effective bending stiffness K^* increases with increase in the trailing edge angle of the flexible plate.

TABLE III. K^* for typical non-uniformly rigid distributions and shape parameter combinations.

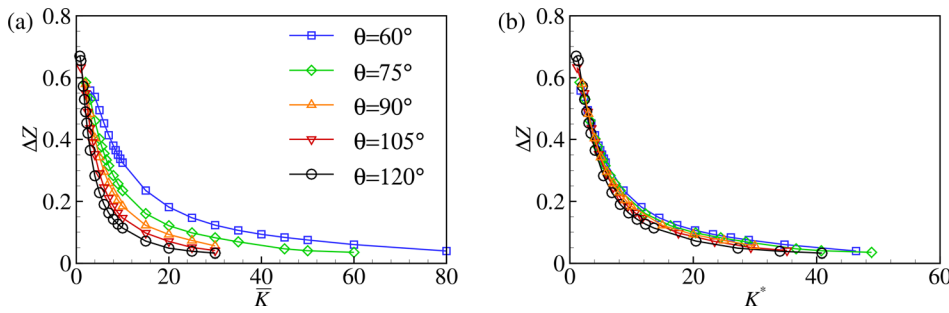| Plate	60°	75°	90°	105°	120°
exp2 ↓	$1.16460\bar{K}$	$1.49702\bar{K}$	$1.73250\bar{K}$	$1.93417\bar{K}$	$2.12789\bar{K}$
exp1 ↓	$0.79397\bar{K}$	$1.09403\bar{K}$	$1.32538\bar{K}$	$1.53814\bar{K}$	$1.76560\bar{K}$
uniform	$0.57978\bar{K}$	$0.81503\bar{K}$	$\bar{K}$	$1.17336\bar{K}$	$1.36184\bar{K}$
exp1 ↑	$0.38384\bar{K}$	$0.54911\bar{K}$	$0.68111\bar{K}$	$0.80651\bar{K}$	$0.94447\bar{K}$
exp2 ↑	$0.08269\bar{K}$	$0.12272\bar{K}$	$0.15536\bar{K}$	$0.18757\bar{K}$	$0.22356\bar{K}$

FIG. 6. Maximum displacement difference ΔZ as a function of (a) the mean bending stiffness $\bar{K}$, and (b) the normalized bending stiffness K^* for uniform flexible plates with different shape parameters.

Therefore, the effective bending stiffness K^* is determined by both the stiffness distribution and the shape parameters.

It is assumed that the maximum lateral displacement difference ΔZ between the leading and trailing edges of the flexible plate during flapping is proportional to the derived tail deformed deflection $w(1)$ of the plate. Through our numerical simulations, we obtain ΔZ as a function of $\bar{K}$ and K^* for different stiffness distribution and the shape parameters. Figure 6 only shows the case of uniform stiffness, and the results for non-uniform stiffness distribution are the same, which will not be described in detail here. It can be seen that for a specific arithmetic mean stiffness $\bar{K}$, the maximum lateral displacement differences ΔZ for flexible plates with different shapes are quite different [see Fig. 6(a)]. When $\bar{K}$ is used, the curve is not well normalized. On the other hand, for a specific effective bending stiffness K^*, plates with different shape parameters correspond to the same ΔZ, and all the curves almost collapse together [see Fig. 6(b)]. In addition, the maximum lateral displacement difference ΔZ is inversely proportional to the effective bending stiffness K^*, which corresponds to Eq. (29). Therefore, the effective bending stiffness K^* can well represent the overall bending stiffness of flexible plates with arbitrary shape and non-uniform stiffness distribution combinations. In this paper, the effective bending

stiffness of rectangular plates with non-uniform stiffness in Ref. 34 is successfully extended to non-uniform plates with arbitrary shape. In the following discussion, the effective bending stiffness K^* will be used as an important parameter to analyze the propulsive performance of flexible plates.

1. Propulsive performance with $\tilde{K}$

The variation trend of mean propulsive velocity and efficiency of flapping plates with effective bending stiffness K^* is shown in Figs. 7 and 8. It is seen that for flexible plates with arbitrary shape and different stiffness distributions, the variation trend of propulsive velocity U and the propulsive efficiency η with K^* is basically consistent with that of uniform case. When the effective bending stiffness K^* is around 4, the maximum propulsion speed U and efficiency η of flexible plates with different stiffness distribution and shape parameters are achieved. Among all the stiffness distributions, the GD mode with the largest standard deviation (exp2 ↑) achieves the largest U and η at the optimal effective bending stiffness K^*. On the other hand, for any specific stiffness distribution, the largest U and η of the flexible plate with an acute trailing edge is better than that of obtuse angle. It should be noted that
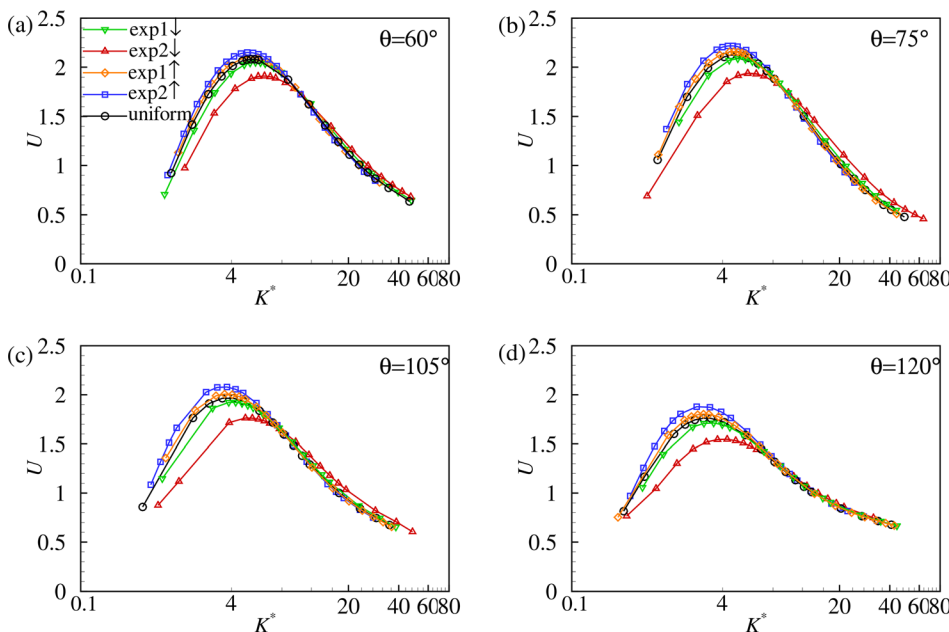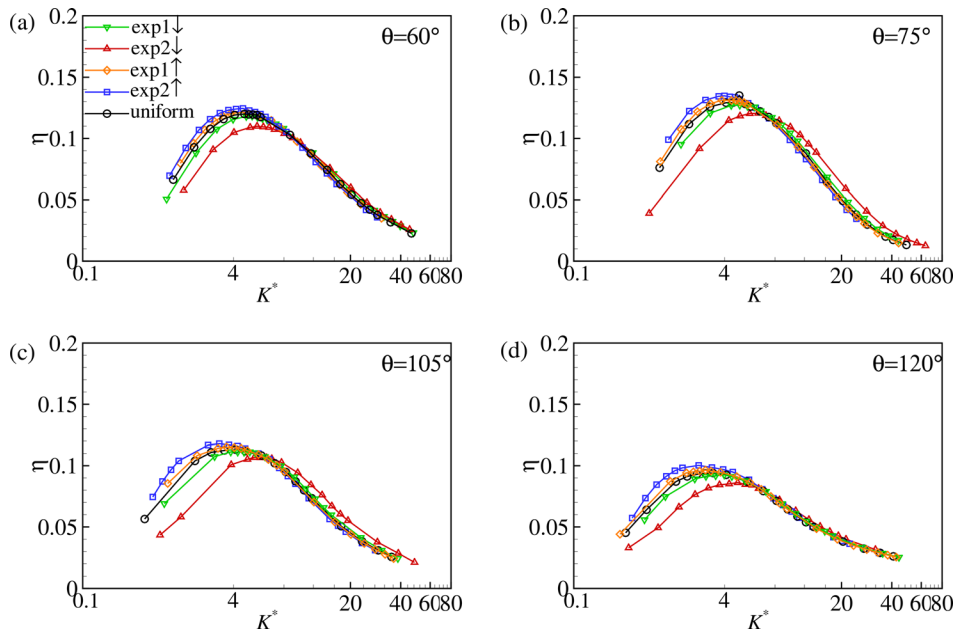

FIG. 7. Propulsive velocity U as a function of K^* of the plate under different stiffness distributions and shape parameter combinations: (a) $\theta = 60°$, (b) $\theta = 75°$, (c) $\theta = 105°$, and (d) $\theta = 120°$.

FIG. 8. Propulsive efficiency η as a function of K^* of the plate under different stiffness distributions and shape parameter combinations: (a) $\theta = 60°$, (b) $\theta = 75°$, (c) $\theta = 105°$, and (d) $\theta = 120°$.

only the bending stiffness is normalized here, the difference of propulsive characteristics well reflects the influence of stiffness distribution and shape parameters.

Now we can reasonably compare the propulsive performance of flapping flexible plates with different stiffness distributions and shape parameters under a specific effective bending stiffness K^*. For the flapping plate with a specific shape parameter, when K^* is small, there is a significant difference in the propulsion performance of flexible plates due to the difference in stiffness distribution. When K^* is large, the propulsive performance curves of different stiffness distributions almost collapse together. When the plate is rigid, the deformation of the plate is almost zero, and the thrust is mainly caused by the leading edge vortex,[49] and the influence of stiffness distribution disappears. On the other hand, for any specific stiffness distribution, when K^* is larger, propulsive velocity U and efficiency η of the flapping flexible plate increases monotonically with increase in the area moment, which increases the thrust on the plate.[55,65] When K^* is small, the propulsive velocity U and efficiency η of the flexible plate with acute trailing edge is better than that with obtuse trailing edge. Here, the propulsive performance of the flexible plate is affected by the flexible deformation and shape parameters. The variation trend of input work W with K^* is similar to that of the propulsive velocity U and efficiency η, which will not be described in detail here.

Therefore, based on the optimal K^*, we find the optimal combination of shape parameters and stiffness distribution. The plate with the GD mode (exp2 ↑) and the trailing edge angle of 75° achieves the best propulsion characteristics among all simulation parameters. Compared with the uniform rectangular plate, the propulsive velocity U and efficiency η are increased by 6.6% and 8.5%, respectively. Compared with the flexible plate with exp2 ↓ and 120° trailing edge angle, the propulsive velocity U and efficiency η are increased by 43.4% and 56.4%, respectively. For rectangular plates, the propulsive velocity U and efficiency η of case exp2 ↑ are only 3% and 4% higher

than those of uniform plates, respectively. Compared with case exp2 ↓, the propulsive velocity U and efficiency η of case exp2 ↑ are only increased by 8% and 4.2%, respectively. It can be seen that a change of plane shape aggravates the difference in propulsion characteristics between the plates.

Strouhal number (St) is an important dimensionless parameter in flapping propulsion, which is defined as

$$St = \frac{fA_w}{U}, \qquad (31)$$

where f is the flapping frequency, A_w is the width of the wake which may be taken as the maximum excursion of the plate trailing edge or twice the amplitude, i.e., $A_w = 2A$, and U is the self-propulsive velocity.[53] Based on investigations of 42 species (birds, bats, insects, sharks, bony fish, and dolphins) in the cruise state, Taylor et $al.$[66] statistically estimated that St lies in the interval $0.2 < St < 0.4$. In this range, the cruise of the flying and swimming animals driven by the wing or tail is likely to have high propulsive efficiency. It can be seen from Figs. 7 and 8 that when the plates have large propulsion speed and efficiency under different parameters, the corresponding effective bending stiffness range is approximately $2 < K^* < 20$. For comparison, Fig. 9 shows the variation of St number with effective bending stiffness K^* for each case. The Strouhal numbers of the majority of our simulations fall into the range of $0.2 < St < 0.4$, which is consistent with the region of high propulsive characteristics of real flapping-based locomotion in nature.

2. Deformation and bending energy

In the process of motion and deformation of the flexible plate, the elastic potential energy can be obtained due to the fluid–structure interaction. In this problem, the tensile deformation of the plate is
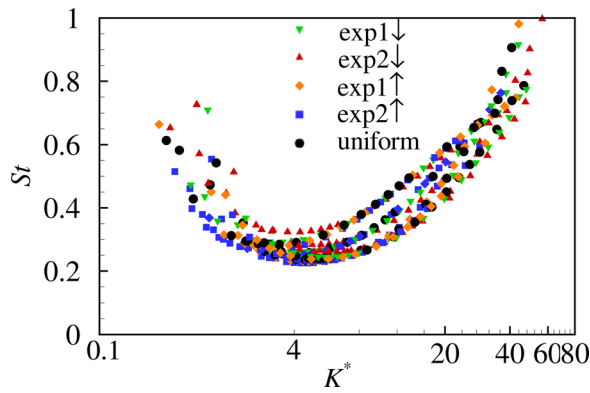
FIG. 9. The Strouhal number St vs the effective bending stiffness K^*.

neglected. The bending energy of a flexible plate is expressed as follows:

$$E_b(t) = K/2 \int\int \sum_{i,j=1}^{2} \gamma_{ij} \partial^2 \mathbf{X}/\partial s_i^2 \cdot \partial^2 \mathbf{X}/\partial s_j^2 \, ds_1 ds_2. \quad (32)$$

Further, the forces acting on the plate and the bending energy of the plate are investigated. Our research focuses on the comparison of optimal propulsive performance for a typical combination of shape parameters and non-uniform stiffness distribution. Some typical cases are chosen to be those at $K^* \approx 4$ since they achieve the best performance. Among them, combination I consists of the plate with exp2 ↑ and a trailing edge angle of 75° and combination II consists of the case with exp2 ↓ and a trailing edge angle of 120°.

The deformation at four typical moments in a flapping cycle, horizontal force, and bending energy of the flexible plate as functions of time are shown in Figs. 10 and 11, respectively. The four typical moments are the instants when the flexible plate is at its maximum thrust or resistance. It can be seen from Fig. 10 that the flexible plate in both cases is in the first-order chordal bending mode. The front area of the plate moves along the front edge, and the rear area is passively deformed under the action of inertial force, elastic force, and the surrounding flow force. Because the head is narrow and soft, and the tail is wide and hard, during the whole flapping period, for the plate combination I from the head, the deformation is larger and the deformation amplitude decreases gradually. On the contrary for the plate combination II, the head deformation is smaller, and the deformation

becomes larger along with the decrease in chord stiffness. From Fig. 11(a), it can be seen that at $t/T \approx 0.25$, the horizontal force F_x of the plate combination I is at the lowest point when the plate is at the moment of maximum thrust. However, when $t/T \approx 0.15$, combination II reaches the maximum thrust, there is a phase difference between the two cases and the thrust in combination I is greater than that in combination II. In addition, combination I achieves greater bending energy [Fig. 11(b)]. The bending energy contained in the plates will be converted into the kinetic energy needed for the plates to move forward. The deformation, force, and bending energy of the upper stroke are similar to those of the lower stroke. Therefore, after a flapping cycle, the plate combination I obtains a larger cruising velocity U, which is consistent with the previous conclusion. The results show that the self-propulsion performance of the flexible plate is closely related to the tangential deformation of the plate, which directly depends on its own stiffness distribution and shape parameters.

3. Vortical structure and pressure distribution

To better understand the inherent mechanism in plates of different parameters, i.e., the above two typical cases with combination I and combination II at optimal effective bending stiffness $K^* = 4$, the connection between vortical structures and pressure distribution on the plate is investigated.

Figure 12 shows the instantaneous vortices of four flexible plates with equal time intervals in a flapping period, which are colored by spanwise vorticity. The vortex structure in the figure is in the form of Q criterion of Jeong and Hussain,[67]

$$Q = \frac{1}{2}(||W||^2 - ||S||^2), \quad (33)$$

where W is the rotation tensor and S is the stretching tensor. When Q is positive, the rotation intensity of the region is higher. On a whole, it can be seen from Fig. 12 that the wake of flapping flexible plate is mainly divided into two discrete vortex structures, and each vortex moves to the downstream independently.[55,68,69] At the moment of $t/T = 0$ [Figs. 12(a) and 12(e)], the flexible plate is at the highest point of heaving motion, and strong vortices are generated at the four edges of the lower side of the plate (referring to the upper side of the plate when $t/T = 0.5$). The vortices induced by the leading edge evolve into leading edge vortices and transport to the trailing edge. Streamwise vortices at the side edge are generated from the upper side of the plate first, and then around the bottom of the plate along the
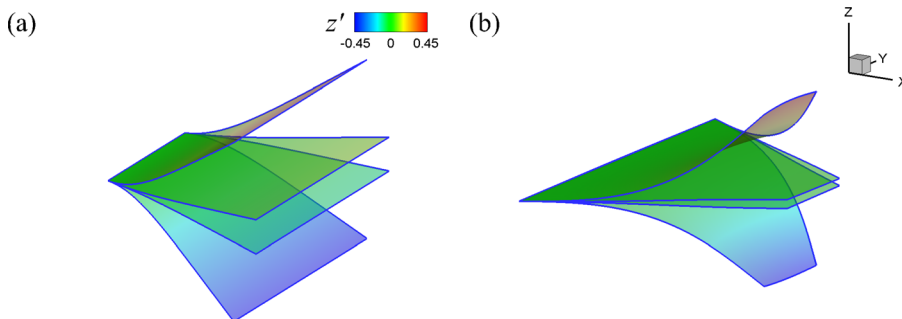
(a) z' -0.45 0 0.45 (b)

FIG. 10. Plate deformation shape at four instances during one flapping cycle. (a) Combination I: exp2 ↑, $\theta = 75°$ and (b) combination II: exp2 ↓, $\theta = 120°$. The selected moment is the instant when the flexible plate is at the maximum thrust or resistance, where $Z' = Z - Z_{leading}$.
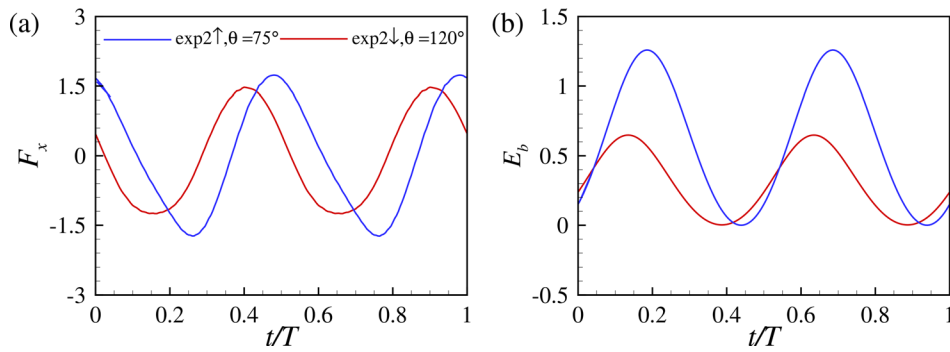
FIG. 11. (a) Evolution of the non-dimensional horizontal force F_x and (b) the bending energy E_b for cases of combination I (blue line) and II (red line) at $K^* \approx 4$.

side edges of both sides due to the pressure difference between the upper and lower surfaces of the plate. In the half flapping period, the side edge vortices are connected with the trailing edge vortices to form a vortex ring, which is transported to the rear of the flow field in an outward expansion trend relative to the propulsion direction, while the upper surface of the plate will regenerate a new vortex structure.

Due to the symmetry of flapping motion, the evolution of the wake vortex in the second half period is similar to that of the first half period.

Now, we focus on the influence of the shape parameters of the flexible plate on the wake vortex structure. Figure 13 shows the wake vortex structure and spanwise vorticity (ω_y) of two groups of flapping plates at $t/T = 0.5$. Some typical structures, such as the leading edge vortex, side vortex, and trailing edge vortex, are labeled as LV, SV, and TV, respectively. Due to the small aspect ratio ($AR = 1$) of the flexible plate in the parameter setting, the distance between the side edge vortices on both sides of the plate is close.
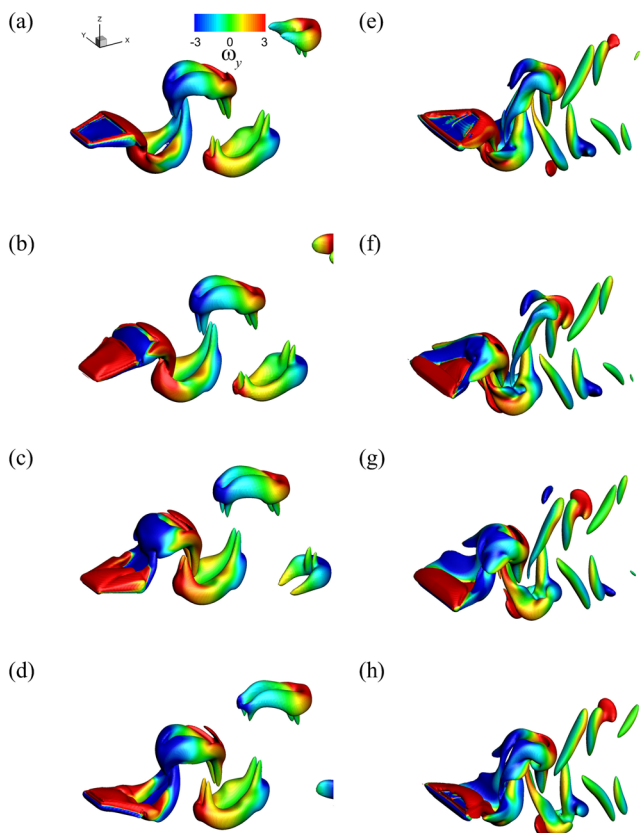

FIG. 12. Snapshots of instantaneous vortical structures: [(a)–(d)] combination I (exp2 ↑, $\theta = 75°$), [(e)–(h)] combination II (exp2 ↓, $\theta = 120°$) with optimal effective bending stiffness $K^* \approx 4$. From top to bottom, it represents specific moments: [(a) and (e)] $t/T = 0$, [(b) and (f)] $t/T = 0.25$, [(c) and (g)] $t/T = 0.5$, and [(d) and (h)] $t/T = 0.75$. In all snapshots, the iso-surface of the Q criterion with $Q = 3$ is shown and it is colored by the spanwise vorticity.
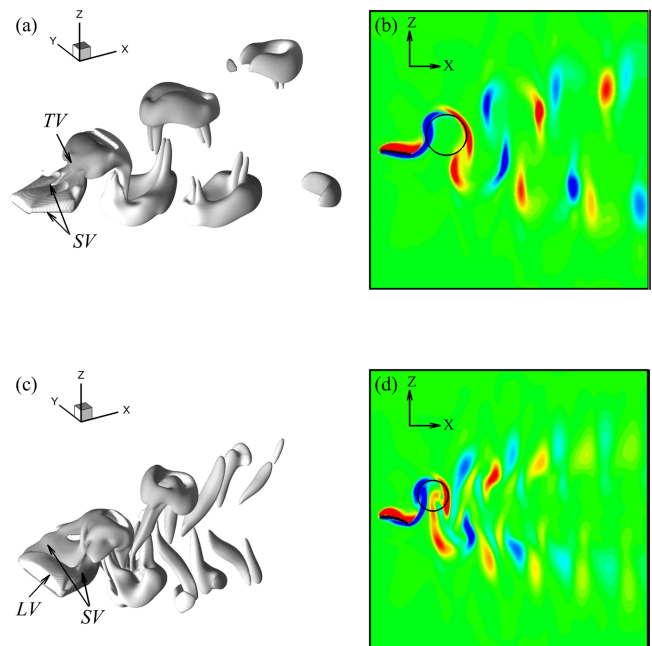

FIG. 13. Snapshots of instantaneous vortical structures and spanwise vorticity (ω_y) on the spanwise symmetry planes for plates with optimal effective bending stiffness $K^* \approx 4$ at the moment $t/T = 0.5$, where LV, SV, and TV represent the leading edge vortex, side edge vortex, and trailing edge vortex, respectively. [(a) and (b)] Combination I and [(c) and (d)] combination II. In all snapshots, the iso-surface of the Q criterion with $Q = 1$ is shown and the range of vorticity ω_y is [−5, 5]. Black circle represents the equivalent vortex ring of vortex structure the equivalent vortex ring of vortex structure.

For combination I, the first-order area moment $\hat{r}$ of the plate is larger—which means narrow in the front and wide in the back [see Fig. 13(a)]. The spanwise vorticity of the leading edge is easy to be transferred to both sides, which weakens the strength of the leading edge vortex, while the wide back enhances the strength of the trailing edge vortex.[70] After shedding from the trailing edge, the vortex mainly appears as a ring structure. There is a strong attached spanwise vortex tube outside the vortex ring, while the residual vortex structure is weak. With the fusion, evolution, and fragmentation of vortex structures, the wake vortex of the flexible plate cannot maintain the ring structure downstream and dissipates gradually. For combination II, the first-order area moment $\hat{r}$ of the plate is smaller, i.e., wide in the front and narrow in the back [Fig. 13(c)]. It can be seen clearly that the leading edge of the flexible plate induces a strong vortex structure. At this time, the two sides of the leading edge vortex melt directly with the side edge vortex at the front end and fall off from the upper side of the flexible plate indirectly, while the side edge vortex at the rear end directly connects and falls off on the plate, replacing the trailing edge vortex and forming an approximate closed vortex ring directly. The wake structure shows that there is no longer a strong spanwise vortex tube outside the vortex ring due to the weak trailing edge vortex. Meanwhile, the strength of the residual vortex tube at the end of the vortex ring is very strong, which is equivalent to the strength of the vortex ring structure at the trailing edge of the flexible plate. When the wake vortex structure is transported backward, the spanwise vortex tube disappears due to viscous dissipation, and only two transverse vortex tubes are left. The spanwise vorticity (ω_y) on the corresponding the spanwise symmetry plane is calculated from Figs. 13(b) and 13(d). It can be seen that the angle between the vortex ring structure and the horizontal direction is basically identical. Compared with combination II, combination I has a larger vortex ring, longer vortex street, and slower vortex dissipation, so the jet momentum generated by wake vortex is larger. According to Newton's third law, combination I would obtain greater forward momentum, which is consistent with the previous results of propulsion characteristics.

Figure 14 shows the instantaneous pressure field along the spanwise section of the flexible plate and the pressure distribution on the upper and lower surfaces of the plate. The corresponding moment is the instant when the maximum thrust appears in each case, i.e., $t/T = 0.25$ and $t/T = 0.15$ in the cases of combination I and II, respectively. It can be seen that the pressure on the lower side of the plate is higher than that on the upper side, and the low pressure area on the

upper surface looks similar. For the lower surface, the pressure distribution is significantly different. The pressure in the middle and rear regions of the plate in combination I is much higher than that of combination II. Therefore, the pressure difference between the upper and lower surfaces of combination I is much larger than that of combination II. On the other hand, the chordwise deformation difference further enhances the forward thrust in combination I. Therefore, combination I obtains better propulsion performance. In conclusion, the change of shape parameters and stiffness distribution of the flexible plate would directly change the deformation and vortex generation of each part of the flexible plate, further affecting the strength of the corresponding parts of the pressure field and wake vortex structure in the flow field, and finally change the stress of the flexible plate.

C. Force analysis

The propulsive performance of flexible plate is closely related to the thrust. The forces experienced by the plates are analyzed to reveal the deformation and propulsion mechanism. Previous studies on flapping flexible wings and plates[71,72] have indicated that flexible deformation plays an important role in determining the thrust and drag. Here, the influence of shape parameters and stiffness distribution of flexible plates on tangential deformation and thrust distribution is discussed quantitatively.

The jump in fluid force across the plate on a Lagrangian point, i.e., F_s, can be decomposed into two parts: one is the normal force F^n in which the pressure component dominates, the other is the tangential force F^τ which comes from viscous effects. These forces are defined as

$$F^n = (F_s \cdot n) \cdot n = (F_x^n, F_y^n, F_z^n), \tag{34}$$

$$F^\tau = F_s - F^n = (F_x^\tau, F_y^\tau, F_z^\tau), \tag{35}$$

where n and τ are the unit normal and tangential vectors, respectively, as shown in Fig. 15(a). The normal force mainly comes from the pressure difference between the upper and lower surfaces of the plate, which provides most of the thrust of the plate forward.

Here the deformation and thrust of two typical examples of combination I and combination II are analyzed for $K^* = 4$. In addition, the rectangular plate is used for comparison. The local slope, normal force, and x component of the normal force along the chord of plate are shown in Figs. 15(b)–15(d), respectively. It should be noted that
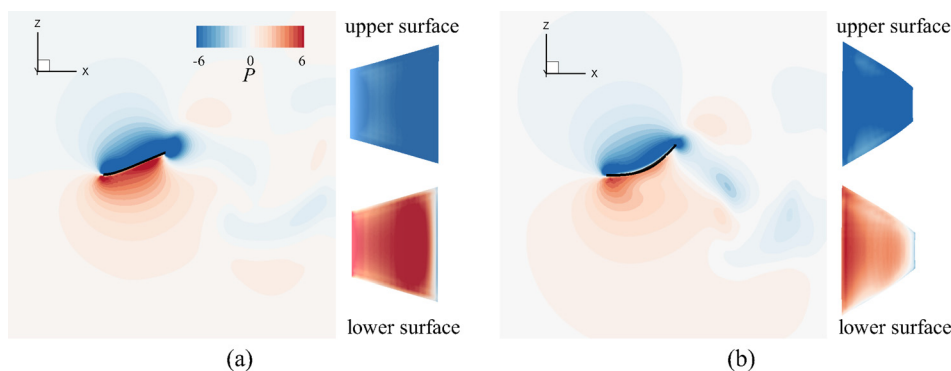

(a)   (b)

FIG. 14. Instantaneous pressure field and pressure distribution along the upper and lower surfaces of a plate on the spanwise symmetry plane at the moment when each case achieves its own largest thrust, where $K^* \approx 4$. (a) Combination I and (b) combination II.
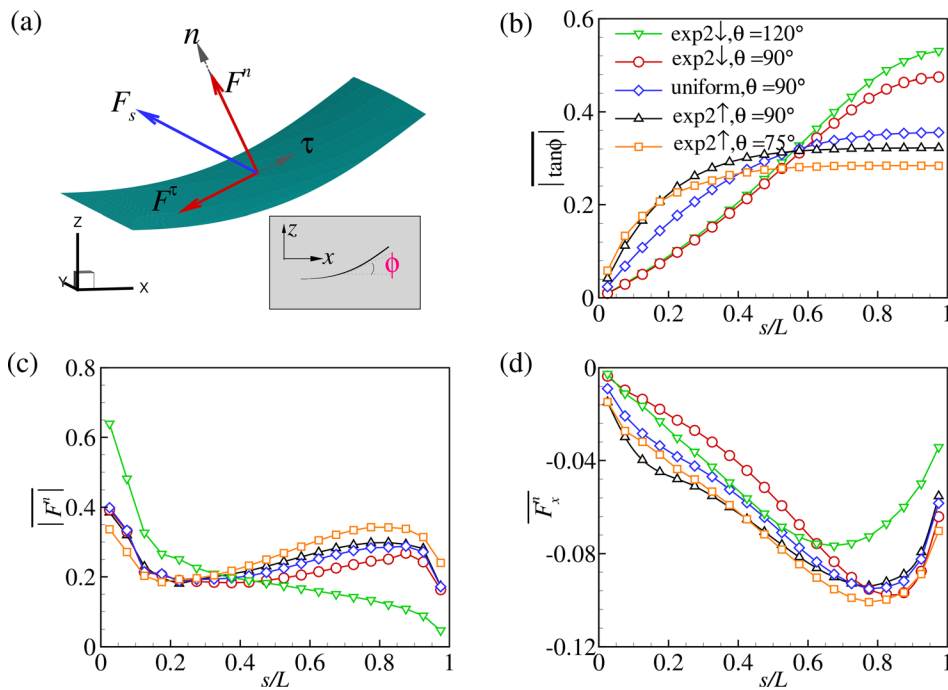
FIG. 15. (a) Schematic diagram for force decomposition, τ and n denote the local tangential and normal directions, respectively. Inset represents the local deflection angle ϕ at the Lagrangian point on the spanwise symmetric plane. (b) Time-averaged absolute slope, (c) time-averaged absolute normal force, and (d) time-averaged F_x^n.

although the overall effective stiffness K^* of the plate is the same, the local effective bending stiffness is different for various cases. It can be seen from Fig. 15(b) that the chordal local slope of the plate is mainly affected by the stiffness distribution. On a whole, for the stiffness distribution exp2 $\downarrow$, in the front region, the local slope is the smallest, and with increase in the chord stiffness, the slope growth rate increases, and when it reaches the rear region, the local slope is the largest. For the stiffness distribution exp2 $\uparrow$, the local slope is the largest in the front area. With increase in the chord stiffness, the slope growth rate gradually decreases until it reaches zero. On the other hand, the influence of shape parameters on the local slope is mainly reflected in the region with small Young's modulus, that is, the back of stiffness distribution exp2 $\downarrow$ and the front of stiffness distribution exp2 $\uparrow$. There is a positive correlation between local effective bending stiffness and spanwise length—for example, the rear part of the stiffness distribution exp2 $\downarrow$ and the front part of exp2 $\uparrow$. The spanwise length of plate $\theta = 120°$ and $\theta = 75°$ is smaller than that of rectangular plate, and the plate is more flexible and the slope is larger.

As the leading edge of the plate is forced to vibrate in the vertical direction, a large load will appear on the head, resulting in a large normal force F^n [see Fig. 15(c)]. For the trailing edge, there is a low pressure region near the vortex region (see Fig. 14), which produces a small normal force F^n. It can be seen that the normal force $|F^n|$ along the chord direction of the plate is mainly affected by the shape parameters. For plate $\theta = 120°$, $|F^n|$ is the largest in the front region. With decrease in the spanwise width, the normal force $|F^n|$ gradually decreases to a minimum in all cases. On the other hand, for plate $\theta = 75°$, the variation trend of $|F^n|$ is just the opposite. In the front region, $|F^n|$ is the smallest, and with increase in the spanwise width, $|F^n|$ gradually increases until it reaches a maximum in all cases. The

horizontal thrust F_x^n is the combined result of local bending deformation and normal force [see Fig. 15(d)]. The total thrust is composed of the accumulation of local thrust F_x^n. Therefore, under the same maximum lateral displacement difference ΔZ between the front and rear edges, the larger bending deformation at the front and the stronger normal force at the rear of plate combination I are accumulated and converted into the maximum total thrust $\overline{F_x^n}$, so as to obtain the optimal propulsion performance. For plate combination II, the bending deformation at the front is small and the normal force at the back is weak, which lead to the minimum total thrust $\overline{F_x^n}$.

V. CONCLUDING REMARKS

In this paper, the numerical simulation of immersed boundary method (IB) coupled with fluid–structure solver is used to study three-dimensional self-propulsive flexible plates, focusing on the influence of shape parameters and chord stiffness distribution of flexible plates on their propulsion performance. The major conclusions are briefly summarized as follows.

First, based on the Euler beam model and normalized bending stiffness of non-uniform rectangular plate, a more general definition of effective bending stiffness K^* including the shape parameters is derived. This model is able to describe the overall bending stiffness reasonably. It is verified that the maximum displacement difference ΔZ between the trailing and leading edges is proportional to the analytical deflection $w(1)$ of the trailing edge of plate. It is found that the propulsion speed and efficiency of the flapping plate mainly depend on the effective bending stiffness, or ΔZ. For the flapping plate with a specific shape parameter, when the effective bending stiffness K^* is small, the stiffness distribution gradually transits from the DD mode to uniform plate mode and then to the GD mode, the propulsion

speed U and efficiency η all increase gradually. When the effective bending stiffness K^* tends to be rigid, the propulsive performance converges gradually. For any specific stiffness distribution, when the effective bending stiffness K^* is larger, the propulsion speed U and efficiency η of flapping flexible plate increase monotonically with increase in the area moment. When the effective bending stiffness K^* is small, the cruising speed U and efficiency η of the flexible plates with acute trailing edge are better than those with obtuse trailing edge.

The shape evolution of wake vortices and the pressure distribution in the near field, upper and lower surfaces of the flexible plate with different shapes and material properties are analyzed. The results show that the shape parameters and stiffness distribution of the flexible plate would directly change the deformation and vortex generation of each part of the plate, and then significantly affect the pressure distribution in the flow field and the strength of the corresponding parts of the wake vortex structure, and finally change the stress of the flexible plate. The relationship between stiffness distribution and shape parameters and local chordal deformation and normal force of flapping plate is revealed, it is found that the flapping flexible plate with increasing stiffness along the chord direction has better propulsive performance when the area moment is larger. These results have significance in guiding optimal design of flexible propulsion systems.

ACKNOWLEDGMENTS

DATA AVAILABILITY

The data that support the findings of this study are available from the corresponding author upon reasonable request.

REFERENCES

[1]J. Katz and D. Weihs, "Hydrodynamic propulsion by large amplitude oscillation of an airfoil with chordwise flexibility," J. Fluid Mech. **88**, 485 (1978).

[2]P. W. Webb, "Form and function in fish swimming," Sci. Am. **251**, 58–68 (1984).

[3]R. M. Alexander, *Principles of Animal Locomotion* (Princeton University Press, 1993).

[4]G. V. Lauder, "Function of the caudal fin during locomotion in fishes: Kinematics, flow visualization, and evolutionary patterns," Am. Zool. **40**, 101 (2000).

[5]A. J. Smits, "Undulatory and oscillatory swimming," J. Fluid Mech. **874**, P1 (2019).

[6]F. E. Fish and G. V. Lauder, "Passive and active flow control by swimming fishes and mammals," Annu. Rev. Fluid Mech. **38**, 193 (2006).

[7]W. Shyy, Y. Lian, J. Tang, D. Viieru, and H. Liu, *Aerodynamics of Low Reynolds Number Flyers* (Cambridge University Press, 2007).

[8]S. Alben, "Optimal flexibility of a flapping appendage in an inviscid fluid," J. Fluid Mech. **614**, 355 (2008).

[9]S. Alben, C. Witt, T. V. Baker, E. Anderson, and G. V. Lauder, "Dynamics of freely swimming flexible foils," Phys. Fluids **24**, 051901 (2012).

[10]M. N. J. Moore, "Analytical results on the role of flexibility in flapping propulsion," J. Fluid Mech. **757**, 599 (2014).

[11]S. Heathcote and I. Gursul, "Flexible flapping airfoil propulsion at low Reynolds numbers," AIAA J. **45**, 1066 (2007).

[12]D. B. Quinn, G. V. Lauder, and A. J. Smits, "Maximizing the efficiency of a flexible propulsor using experimental optimization," J. Fluid Mech. **767**, 430 (2015).

[13]D. Floryan and C. W. Rowley, "Clarifying the relationship between efficiency and resonance for flexible inertial swimmers," J. Fluid Mech. **853**, 271 (2018).

[14]B. Yin and H. X. Luo, "Effect of wing inertia on hovering performance of flexible flapping wings," Phys. Fluids **22**, 111902 (2010).

[15]C.-K. Kang, H. Aono, C. E. S. Cesnik, and W. Shyy, "Effects of flexibility on the aerodynamic performance of flapping wings," J. Fluid Mech. **689**, 32 (2011).

[16]X. J. Zhu, G. W. He, and X. Zhang, "How flexibility affects the wake symmetry properties of a self-propelled plunging foil," J. Fluid Mech. **751**, 164 (2014).

[17]A. P. Hoover, R. Cortez, E. D. Tytell, and L. J. Fauci, "Swimming performance, resonance and shape evolution in heaving flexible panels," J. Fluid Mech. **847**, 386 (2018).

[18]N. Arora, C.-K. Kang, W. Shyy, and A. Gupta, "Analysis of passive flexion in propelling a plunging plate using a torsion spring model," J. Fluid Mech. **857**, 562 (2018).

[19]H. Z. Hu, J. S. Wang, Y. K. Wang, and H. B. Dong, "Effects of tunable stiffness on the hydrodynamics and flow features of a passive pitching panel," J. Fluids Struct. **100**, 103175 (2021).

[20]K. N. Lucas, N. Johnson, W. T. Beaulieu, E. Cathcart, and J. H. Costello, "Bending rules for animal propulsion," Nat. Commun. **5**, 3293 (2014).

[21]M. J. McHenry, C. A. Pell, and J. H. Long, Jr., "Mechanical control of swimming speed: Stiffness and axial wave form in undulating fish models," J. Bionic Eng. **198**, 2293 (1995).

[22]C. Zuo and H. Jiang, "Modeling and analysis of a swimming tincaeus with bio-inspired stiffness profile," IEEE International Conference on Robotics and Biomimetics (2015).

[23]A. K. Kancharala and M. K. Philen, "Optimal chordwise stiffness profiles of self-propelled flapping fins," Bioinspir. Biomim. **11**, 056016 (2016).

[24]Y. Luo, Q. Xiao, G. Shi, G. Pan, and D. Chen, "The effect of variable stiffness of tuna-like fish body and fin on swimming performance," Bioinspir. Biomim. **16**, 016003 (2020).

[25]R. J. Zhu, J. S. Wang, H. B. Dong, and H. Bart-Smith, "Effects of chordwise non-uniform stiffness on propulsive performance of passively-flexing square foil," AIAA Paper No. 2020-0804, 2020.

[26]R. J. Zhu, J. S. Wang, H. B. Dong, and H. Bart-Smith, "Effects of chordwise or spanwise non-uniform stiffness on propulsive performance of square foil," AIAA Paper No. 2021-1085, 2021.

[27]D. Fernández-Gutiérrez and W. M. van Rees, "Effect of leading-edge curvature actuation on flapping fin performance," J. Fluid Mech. **921**, A22 (2021).

[28]K. N. Lucas, P. J. Thornycroft, B. J. Gemmell, S. P. Colin, J. H. Costello, and G. V. Lauder, "Effects of non-uniform stiffness on the swimming performance of a passively-flexing, fish-like foil model," Bioinspir. Biomim. **10**, 056019 (2015).

[29]M. N. J. Moore, "Torsional spring is the optimal flexibility arrangement for thrust production of a flapping wing," Phys. Fluids **27**, 091701 (2015).

[30]K. Shoele and Q. Zhu, "Leading edge strengthening and the propulsion performance of flexible ray fins," J. Fluid Mech. **693**, 402 (2012).

[31]K. Shoele and Q. Zhu, "Performance of a wing with nonuniform flexibility in hovering flight," Phys. Fluids **25**, 041901 (2013).

[32]T. T. Nguyen, D. Shyam Sundar, K. S. Yeo, and T. T. Lim, "Modeling and analysis of insect-like flexible wings at low Reynolds number," J. Fluids Struct. **62**, 294 (2016).

[33]Z. Peng, G. J. Elfring, and O. S. Pak, "Maximizing propulsive thrust of a driven filament at low Reynolds number via variable flexibility," Soft Matter **13**, 2339 (2017).

[34]W. J. Wang, H. B. Huang, and X.-Y. Lu, "Optimal chordwise stiffness distribution for self-propelled heaving flexible plates," Phys. Fluids **32**, 111905 (2020).

[35]G. Y. Shi, Q. Xian, and Q. Zhu, "Effects of time-varying flexibility on the propulsion performance of a flapping foil," Phys. Fluids **32**, 121904 (2020).

[36]T. Van Buren, D. Floryan, D. Brunner, U. Senturk, and A. J. Smits, "Impact of trailing edge shape on the wake and propulsive performance of pitching panels," Phys. Rev. Fluids **2**, 014702 (2017).

[37]P. W. Webb, "Effects of partial caudal-fin amputation on the kinematics and metabolic rate of underyearling sockeye salmon (*Oncorhynchus Nerka*) at steady swimming speeds," J. Exp. Biol. **59**, 565 (1973).

[38]V. C. Sambilay, "Interrelationships between swimming speed, caudal fin aspect ratio and body length of fishes," Fishbyte **8**, 16–20 (1990); available at https://hdl.handle.net/20.500.12348/3181.

[39]G. Karpouzian, G. Spedding, and H. K. Cheng, "Lunate-tail swimming propulsion. Part 2. Performance analysis," J. Fluid Mech. **210**, 329 (1990).

[40]J. T. King, R. Kumar, and M. A. Green, "Experimental observations of the three-dimensional wake structures and dynamics generated by a rigid, bioinspired pitching panel," Phys. Rev. Fluids **3**, 034701 (2018).

[41]M. G. Chopra and T. Kambe, "Hydrodynamics of lunate-tail swimming propulsion. Part 2," J. Fluid Mech. **79**, 49 (1977).

[42]M. A. Green, C. W. Rowley, and A. J. Smits, "The unsteady three-dimensional wake produced by a trapezoidal pitching panel," J. Fluid Mech. **685**, 117 (2011).

[43]G.-J. Li, L. D. Zhu, and X.-Y. Lu, "Numerical studies on locomotion performance of fish-like tail fins," J. Hydrodyn. B **24**, 488 (2012).

[44]Y. Jin, J.-T. Kim, L. Hong, and L. P. Chamorro, "Flow-induced oscillations of low-aspect-ratio flexible plates with various tip geometries," Phys. Fluids **30**, 097102 (2018).

[45]G. J. Li, G. Kemp, R. K. Jaiman, and B. C. Khoo, "A high-fidelity numerical study on the propulsive performance of pitching flexible plates," Phys. Fluids **33**, 051901 (2021).

[46]L. Yao, C. Hefler, W. Shyy, and H. H. Qiu, "Effects of gradual flexibility and trailing edge shape on propulsive performance of pitching fins," Phys. Fluids **33**, 071901 (2021).

[47]G. V. Lauder, J. Lim, R. Shelton, C. Witt, E. Anderson, and J. L. Tangorra, "Robotic models for studying undulatory locomotion in fishes," Mar. Technol. Soc. J. **45**, 41 (2011).

[48]J. Ryu, S. G. Park, W.-X. Huang, and H. J. Sung, "Hydrodynamics of a three-dimensional self-propelled flexible plate," Phys. Fluids **31**, 021902 (2019).

[49]C. Zhang, H. Huang, and X.-Y. Lu, "Effect of trailing-edge shape on the self-propulsive performance of heaving flexible plates," J. Fluid Mech. **887**, A7 (2020).

[50]S. Michelin and S. G. Llewellyn Smith, "Resonance and propulsion performance of a heaving flexible wing," Phys. Fluids **21**, 071902 (2009).

[51]Z.-R. Peng, H. B. Huang, and X.-Y. Lu, "Collective locomotion of two closely spaced self-propelled flapping plates," J. Fluid Mech. **849**, 1068 (2018).

[52]B. S. H. Connell and D. K. P. Yue, "Flapping dynamics of a flag in a uniform stream," J. Fluid Mech. **581**, 33 (2007).

[53]R.-N. Hua, L. D. Zhu, and X.-Y. Lu, "Locomotion of a flapping flexible plate," Phys. Fluids **25**, 121901 (2013).

[54]C. P. Ellington, "The aerodynamics of hovering insect flight. II. Morphological parameters," Philos. Trans. R. Soc. B **305**, 17–40 (1984).

[55]G.-J. Li, N. S. Liu, and X.-Y. Lu, "Dynamic performance and wake structure of flapping plates with different shapes," Acta Mech. Sin. **30**, 800 (2014).

[56]S. Y. Chen and G. D. Doolen, "Lattice Boltzmann method for fluid flows," Annu. Rev. Fluid Mech. **30**, 329 (1998).

[57]J. F. Doyle, *Nonlinear Analysis of Thin-Walled Structures: Statics, Dynamics, and Stability* (Springer, 2001).

[58]C. S. Peskin, "The immersed boundary method," Acta Numer. **11**, 479 (2002).

[59]R. Mittal and G. Iaccarino, "Immersed boundary methods," Annu. Rev. Fluid Mech. **37**, 239 (2005).

[60]C. Tang, H. Huang, P. Gao, and X.-Y. Lu, "Self-propulsion of a flapping flexible plate near the ground," Phys. Rev. E **94**, 033113 (2016).

[61]L. Wang, Z. Fang, R.-N. Hua, and Z.-R. Peng, "Numerical simulations of an inverted flexible plate in linear shear flows," Phys. Fluids **32**, 043104 (2020).

[62]Z. Guo, C. Zheng, and B. Shi, "Discrete lattice effects on the forcing term in the lattice Boltzmann method," Phys. Rev. E **65**, 046308 (2002).

[63]R.-N. Hua, L. D. Zhu, and X.-Y. Lu, "Dynamics of fluid flow over a circular flexible plate," J. Fluid Mech. **759**, 56 (2014).

[64]W.-X. Huang and H. J. Sung, "Three-dimensional simulation of a flapping flag in a uniform flow," J. Fluid Mech. **653**, 301 (2010).

[65]G. Luo and M. Sun, "The effects of corrugation and wing planform on the aero-dynamic force production of sweeping model insect wings," Acta Mech. Sin. **21**, 531 (2005).

[66]G. K. Taylor, R. L. Nudds, and A. L. R. Thomas, "Flying and swimming animals cruise at a Strouhal number tuned for high power efficiency," Nature **425**, 707 (2003).

[67]J. Jeong and F. Hussain, "On the identification of a vortex," J. Fluid Mech. **285**, 69 (1995).

[68]H. Dong, R. Mittal, and F. M. Najjar, "Wake topology and hydrodynamic performance of low-aspect-ratio flapping foils," J. Fluid Mech. **566**, 309 (2006).

[69]J. H. J. Buchholz and A. J. Smits, "The wake structure and thrust performance of a rigid low-aspect-ratio pitching panel," J. Fluid Mech. **603**, 331 (2008).

[70]K. Taira and T. Colonius, "Three-dimensional flows around low-aspect-ratio flat-plate wings at low Reynolds numbers," J. Fluid Mech. **623**, 187 (2009).

[71]B. Thiria and R. Godoy-Diana, "How wing compliance drives the efficiency of self-propelled flapping flyers," Phys. Rev. E **82**, 015303 (2010).

[72]S. Ramananarivo, R. Godoy-Diana, and B. Thiria, "Rather than resonance, flapping wing flyers may play on aerodynamics to improve performance," Proc. Natl. Acad. Sci. U. S. A. **108**, 5964 (2011).